RESEARCH ARTICLE | APRIL 03 2025

Turbulence flow field in a four-fan stirred combustion furnace

Huina Guo (郭慧娜) ; Xinde Zhang (张新德); Zhoutao Cen (岑周涛); Xin Li (李欣); Yuxin Wu (吴玉新)

Physics of Fluids 37, 045119 (2025)
https://doi.org/10.1063/5.0265341

Physics of Fluids ARTICLE pubs.aip.org/aip/pof

Turbulence flow field in a four-fan stirred combustion furnace

Cite as: Phys. Fluids **37**, 045119 (2025); doi: 10.1063/5.0265341
Submitted: 13 February 2025 · Accepted: 18 March 2025 ·
Published Online: 3 April 2025

Huina Guo (郭慧娜),[1] Xinde Zhang (张新德),[2] Zhoutao Cen (岑周涛),[1] Xin Li (李欣),[1] and Yuxin Wu (吴玉新)[1,3,a)]

AFFILIATIONS

[1]Department of Energy and Power Engineering, Tsinghua University, Key Laboratory of Thermal Science and Power Engineering, Ministry of Education, Beijing 100084, China;
[2]Department of Environmental Science and Engineering, North China Electric Power University, Baoding 071003, China
[3]Low Carbon Energy and CCUS Research Center, Institute for Carbon Neutrality, Tsinghua University, Beijing 100084, China

[a)]**Author to whom correspondence should be addressed:** wuyx09@mail.tsinghua.edu.cn. **Tel.:** +86-10-62799641. **Fax:** +86-10-62781743

ABSTRACT

This study comprehensively investigates the turbulence flow within a four-fan stirred combustion furnace using experimental and numerical approaches. To analyze the impact of turbulence on fuel combustion, a prerequisite is to accurately obtain the control rules before fuel combustion. This study established a high-frequency sampling method using a hot-wire anemometer to quickly test the homogeneous and isotropic turbulence (HIT) region and employing a continuous laser combined with a high-speed camera to achieve particle image velocimetry measurements of the central two-dimensional flow field. A steady simulation combining the realizable k–ε model with a multiple reference frame was performed to further analyze the three-dimensional flow field. The results show that the adopted method has high accuracy. Within a central spherical region of approximately 40 mm, the flow field exhibited HIT characteristics, with turbulent fluctuation velocity u_{rms} varying linearly with fan speed ω ($u_{rms} = 0.000\,814\ \omega$). Integral eddy length remains around 14 mm, while smaller-scale Taylor and Kolmogorov eddy significantly decreased with increasing ω. Full-field simulations reveal that the highest turbulence kinetic energy occurred at the intersection of adjacent fan flows. Additionally, the study explored the effect of a 4 mm glass bead on flow field, revealing a rebound effect on mean velocity and a reduction in u_{rms} near the bead. The boundary layer thickness decreases at higher fan speed but remains on the order of particle radius 2 mm. These findings provide a foundation for future research on the role of turbulence lack of mean flow on combustion.

NOMENCLATURE

D	Internal cavity diameter (mm)
E	Induced voltage (V)
f	Frame rate (Hz)
HIT	Homogeneous and isotropic turbulence
HWA	Hot-wire anemometer
k	Turbulent kinetic energy (m^2/s)
L	Internal cavity length or integral length (mm)
LDV	Laser Doppler velocimetry
LES	Large eddy simulation
L_{ux}	Longitudinal integral length of u
L_{vy}	Longitudinal integral length of v
N	Image number
r	Radius (mm)
PIV	Particle image velocimetry
R	Spatial resolution (μm/pixel)
RANS	Reynolds averaged Navier–Stokes
Re_λ	Taylor Reynolds number
Re_L	Turbulent Reynolds number
RSM	Reynolds stress model
R_{uu}	Velocity correlation coefficient of u
R_{vv}	Velocity correlation coefficient of v
u_{ave}	Average velocity (m/s)
u_{rms}	Fluctuating velocities (m/s)
U_{eff}	Effective cooling speeds (m/s)
Δt	Inter-frame time (s)
t	Exposure time (μs)
v	Air kinematic viscosity (m^2/s)
v_{ave}	Average velocity, m/s
v_{max}	Maximum speed (m/s)
v_{rms}	Fluctuating velocities (m/s)

Vel_{ave}	Mean velocity (m/s)
Δx	Pixel size of the interrogation window (pixels)
ε	Dissipation rate (m^2/s^3)
η	Kolmogorov eddy scale (μm)
λ	Taylor eddy scale (mm)
τ_L	Integral eddy time scale (ms)
τ_λ	Taylor eddy time scale (ms)
τ_η	Kolmogorov eddy time scale (ms)
μ	Air dynamic viscosity (Pa·s)
ω	Fan rotational speed (r/min)

Subscripts

ave	Average
eff	Effective
max	Maximum
rms	Root mean square

I. INTRODUCTION

Combustion processes typically occur in strong turbulent environments with complex interactions with flow, heat transfer, and chemical reactions in actual industrial facilities. Turbulent flow affects the combustion behavior from many aspects. For gas combustion,[1,2] turbulent fluctuations stretch the flame front, alter the flame structure, and increase the fuel consumption rate. In the case of liquid fuel combustion,[3–7] turbulent fluctuations enhance droplet evaporation rates and change the spatial distribution of vapor. For solid fuels such as coal and biomass,[8–11] turbulence alters ignition behavior and shortens burnout times. Therefore, many research works have focused on the effect of turbulence on fuel combustion. To achieve this, it is necessary to construct an experimental device capable of generating turbulence. The fundamental assumption in turbulence theory is homogeneous and isotropic turbulence (HIT). Many researchers have conducted theoretical studies and established scaling laws, forming the cornerstone of various theoretical research methods, such as large eddy simulation (LES) and Reynolds averaged Navier–Stokes (RANS). HIT has the same statistical characteristics in all directions without mean flow. Conducting experiments in such environment to study the impact of turbulence can avoid the complexity introduced by anisotropy or inhomogeneity, and its mathematical treatment and experimental design are relatively simple and controllable. Therefore, studying the impact of turbulence on fuel combustion in HIT is the most ideal method.

Multiple opposed fans, speakers, grids, and jets are usually symmetrically arranged inside a closed chamber to form the collision of jets to generate HIT[12–18] with the multi-fan opposed method being the most widely used due to its simplicity of control. Such devices proposed by Semenov[19] can produce reasonable HIT in the central zone of a closed chamber if well designed. The turbulent flow characteristics, including the mean velocity u_{ave}, v_{ave}, turbulence fluctuation velocity u_{rms}, v_{rms}, dissipation rate ε and eddy scale, mainly depend on the chamber size and fan geometric features (i.e., impeller size, blades number, pitch angle, etc.). Even with the same chamber and fan size, changing the number of blades and pitch angle can result in HIT with different eddy scales.[20] Therefore, a detailed and accurate description of the flow field characteristics prior to fuel combustion is a prerequisite for subsequent combustion–turbulence interaction analysis.

The experimental methods for flow field measurement mainly include hot-wire anemometers (HWA),[21,22] particle image velocimetry (PIV),[1,23,24] and laser Doppler velocimetry (LDV).[25,26] HWA is widely used for turbulence characterization because of its high temporal resolution (up to 100 kHz), simultaneous three-dimensional measurement, and low interference with the flow field. The principle is to place an electrically heated wire in the flow field, and the control circuit will change the current according the flow velocity to ensure the constant wire temperature. The response of hot wire to flow velocity is directionally selective, and different angles between the flow field and the wire will lead to different cooling effects. Therefore, HWA is thought to be unsuitable for the HIT measurements and only used in the flow field with a mean flow, such as in wind tunnels and grid turbulence. Although it is impractical to quantitatively measure the turbulent fluctuation speed in HIT using HWA, the directional sensitivity of HWA may be exploited to place hot wires in different directions for a quick assessment of the isotropic properties in the chamber. However, the applicability of this approach needs to be verified.

With the advancement of optical diagnostic technology, PIV and LDV have been adopted for HIT measurements. LDV typically provides high-frequency single-point data, whereas PIV captures planar measurements, with the sampling frequency depending on the laser frequency. Commonly used pulsed lasers measure at 15 Hz, while high repetition rate laser can reach up to 10 kHz, capable of capturing the details of rapidly changing flow fields but at a high cost. The measurement method combining a continuous laser with a high-speed camera features high temporal resolution, simplified optical system, and low cost, making it a viable and cost-effective approach for high-frequency PIV measurements, especially in the hydrodynamics research.[27,28] A well-designed multi-fan opposed chamber with its relatively low instantaneous velocity and lack of mean flow in statistics is conducive to applying a continuous laser combined with a high-speed camera to achieve high-frequency PIV and capture the continuous motion of turbulence eddies. No related studies have attempted this approach currently, and its applicability and key parameters in HIT measurements are worth investigating.

Due to the limited field of view and velocity range in optical PIV measurement, computational fluid dynamics (CFD) methods provide a feasible complementary research path to analyze the 3D velocity information in the full flow field within the chamber. So far, there have been few related research reports. Zhang *et al.*[29] and Bonhomme *et al.*[30] both utilized LES to simulate the turbulence characteristics of eight- and six-fan opposed chamber, because LES considers the motion at the sub-grid scale and is more accurate for turbulence studies. However, the number of grids is as high as 8.6×10^6 and 40×10^6, resulting in computationally intensive solutions, even though a parallel multi-domain strategy is adopted for partitioned calculation. Morsy and Yang[31] applied the RANS method to simulate the entire flow field in a four-fan combustion chamber, comparing the computational results of the Standard k–ε model, RNG k–ε model, and Reynolds stress model (RSM) using 8×10^6 grids. They concluded that the RSM model had better solution performance, and elevating temperature and pressure had a minor impact on the turbulent fluctuation velocity. However, all the aforementioned studies conducted transient calculations, which demand substantial computational resources. The steady RANS method, on the other hand, requires fewer grids and computational resources, while its performance in simulating this particular

device needs further investigation, which is crucial for accurately and rapidly detecting the flow field characteristics with reduced computational resource.

In previous studies along this research path, after the flow field characteristics are characterized, a millimeter-sized fuel particle is placed in the central region of the multi-fan opposed device for further evaporation or combustion experiments. Implanting a particle into HIT flow will affect the flow field and the velocity boundary layer around the particle, especially for the case of placing a millimeter-sized solid fuel particle. Verwey and Birouk[32] studied the modulation effect of a small particle $d/\eta < 10$ on HIT flow and found that near-surface dissipation increases and kinetic energy decreases, but speculated that this effect could be negligible when $d/\lambda \sim 1$. Hoque *et al.*[33] investigated the modulation of a 1–8 mm glass particle on grid turbulence and found a critical ratio $d/L \sim 0.41$ that demarcated the attenuation and enhancement of turbulence intensity. There is still a lack of more intuitive analysis of the velocity around a larger particle. Therefore, it is necessary to carry out PIV measurements before and after the particle implantation to compare the effect of particle.

In summary, this paper constructs a novel furnace capable of generating a high-temperature environment of 900 °C to study the impact of turbulence on solid fuel combustion. Due to the limitations of heating and sealing, only four fans can be symmetrically arranged in the cylindrical combustion chamber. This study aims to investigate the flow field formed by the rotation of a limited number of fans through experimental and simulation methods and to verify whether the central area meets the standards of HIT. First, the directional sensitivity of HWA is utilized to quickly assess the flow uniformity and isotropy. A continuous laser combined with a high-speed camera is designed to capture the transient continuous motion of eddies, achieving high-frequency PIV measurement and quantifying the average velocity, turbulent fluctuation velocity, and eddy spatiotemporal scale. In addition, the turbulent flow before and after the implantation of a millimeter-sized glass bead is analyzed to compare the impact of particles as well as the velocity boundary. A steady-state RANS simulation is constructed to analyze the three-dimensional flow field characteristics in the combustion chamber. This paper also comprehensively evaluates the applicability of the aforementioned research methods.

II. EXPERIMENTAL AND SIMULATION METHODS

A. Experimental setup

The high-temperature turbulent combustion furnace equipped with four axial-flow fans is designed to investigate the effect of turbulence on combustion characteristics of solid fuels in an air or oxygen-rich atmosphere, as shown in Fig. 1. The setup primarily consists of an electric heating system, an electric motor and fan rotation system, a cooling-water circulation system, a vacuum system, a gas supply and exhaust system, and an optical measurement system. The inner cavity is cylindrical with dimensions of $D = 280$ mm and $L = 240$ mm. High-quality chromium–molybdenum–aluminum alloy resistance wires are arranged around the combustion chamber to heat the internal gas to 900 °C. Four sealed motors (green parts in Fig. 1) are symmetrically arranged on the furnace by flanges and connected with four axial fans inside the furnace to disturb the gas inside the furnace and create turbulence. The fan impeller has a diameter of 90 mm and a thickness of 33.14 mm, is designed with five blades made from high-temperature nickel-based alloy, and can operate safely at temperatures up to 1200 °C. The distance between the two opposing fans is 160 mm. The fan speed can be precisely controlled by adjusting the power frequency through a frequency converter. The slits on the left and right sides of the furnace are 10×50 mm^2, and the quartz window at the front of the furnace is 80 mm in diameter, facilitating the laser pathway and optical observations. The cooling-water cycle cools both the furnace and motor to remove heat in time.

This study was conducted in an ambient air at normal temperature and pressure, and the fan rotation speed range is summarized in Table I. The decision to conduct flow field experiments at room temperature is to elucidate the flow characteristics under normal conditions and reasonably extrapolate to high-temperature scenarios. As supported by the references on this type of device,[24,31,34,35] the turbulent fluctuation velocity control law $u_{\mathrm{rms}} = f(\omega)$ and the integral eddy scale L are determined by the design characteristics of the device. While temperature variations alter fluid properties (kinematic viscosity ν and density ρ) thereby affecting the turbulent Reynolds number and spatiotemporal scales of Taylor eddy and Kolmogorov eddy, the governing laws of u_{rms} and integral eddy scale remain temperature-invariant. This fundamental decoupling ensures that the turbulence control principles derived from room-temperature experiments remain valid over a wide temperature range.

B. High-frequency PIV measurement method

Continuous lasers and high-speed cameras are key components in PIV research. The continuous laser used in this study is produced by TAIKE Technology Co., Ltd., with a power of 10 W, capable of generating a Gaussian beam spot with a diameter of approximately 3 mm. According to the principle of Gaussian beam propagation, the divergence angle is inversely proportional to the waist diameter, and the Rayleigh range is directly proportional to the square of the waist diameter. Therefore, the collimation and modulation capabilities of a small spot beam are limited. It was found during the modulation process that without expanding the laser beam, it is difficult to shape it into a planar laser sheet with a thickness of about 0.5 mm. Consequently, based on the propagation principle of Gaussian beams, the optical path was designed as shown in Fig. 1, shaping the laser into a parallel sheet light source with a height of 40 mm and a thickness of 0.5 mm, which enters the furnace through the narrow slit on the left side of the furnace. The high-speed camera used is the Pco.dimax HS4, which has a maximum frame rate of 7039 fps at a resolution of 1000×1000. Due to the presence of electric heating wires in the furnace, tracer particle adhesion is inevitable during the experiment. Therefore, SiC solid tracer particles with a diameter of 1 μm were chosen. To estimate the tracer particle tendency to follow the surrounding flow, the Stokes number St is defined as the ratio of the relaxation time of the tracer particle to a characteristic time of the flow

$$St = \tau_{\mathrm{p}}/\tau_{\mathrm{f}}, \tag{1}$$

$$\tau_{\mathrm{p}} = \frac{\rho_{\mathrm{p}}}{18\mu} d_{\mathrm{p}}^2, \tag{2}$$

where ρ_{p} represents the tracer density, 3200 kg/m^3; μ is the dynamic viscosity of air, 1.85×10^{-5} Pa·s; the flow characteristic time can be inferred as the Kolmogorov timescale τ_η. In this way, St is estimated to be 0.012 at 1000 r/min and 0.16 at 5000 r/min. For $St < 0.2$, tracer particles are expected to closely track the flow, with slip velocity errors

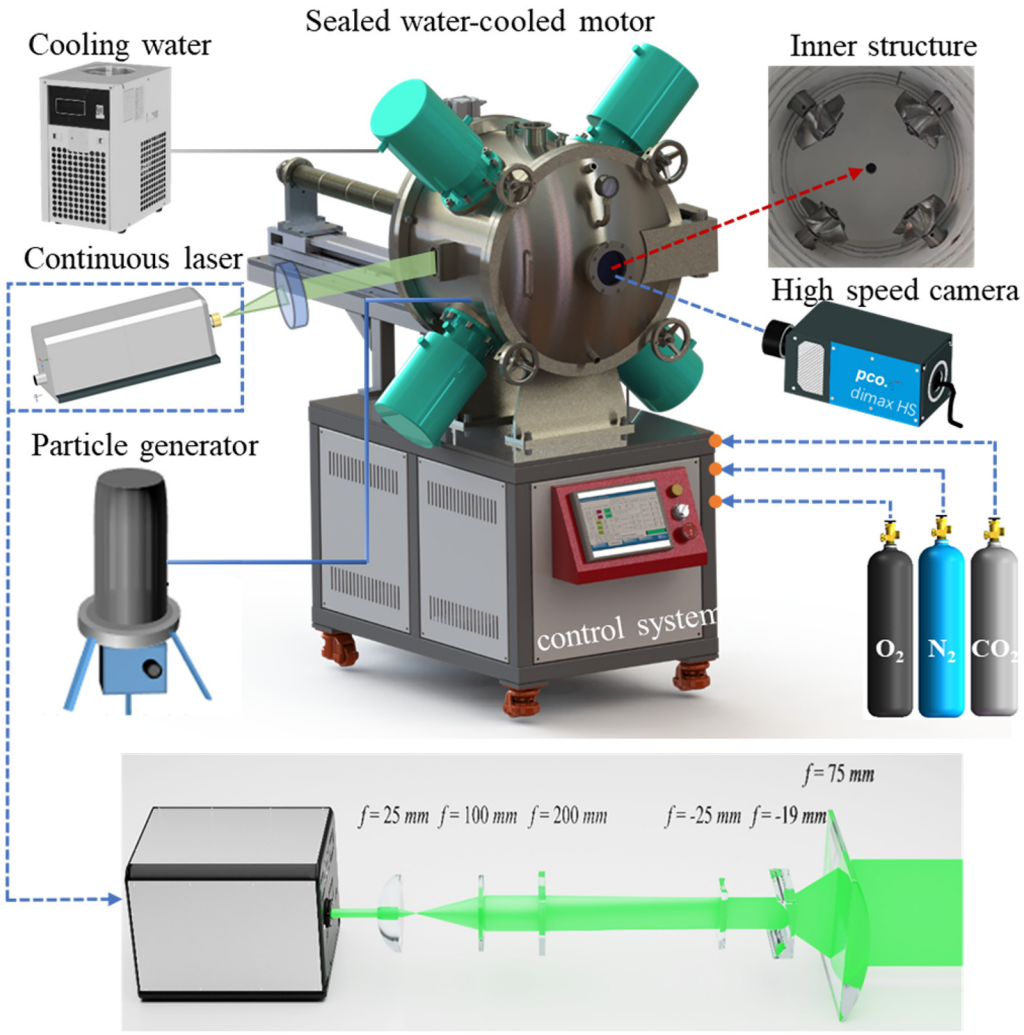

FIG. 1. Schematic diagram of the high-temperature turbulent combustion furnace.

below 2%.[36] PIVlab package in Matlab software is employed for cross correlation processing of the particle images.

The working mode of PIV using a continuous laser and a high-speed camera is different from that of a high repetition rate pulsed laser, as shown in Fig. 2. The main difference is that the inter-frame time Δt is no longer determined by the laser, but is equal to the reciprocal of the high-speed camera's frame rate f, as

$$\Delta t = 1/f. \tag{3}$$

Therefore, the higher the flow velocity, the higher the required frame rate and the shorter the exposure time needed to avoid particle trailing and ensure that the particle displacement in consecutive frames always remains within 1/4 of the interrogation window Δx. However, the frame rate and image pixel size of the high-speed camera are mutually constrained. Increasing the frame rate means reducing the image pixels, which may reduce the spatial resolution.

According to the PIV measurement technical guidelines, the upper limit of the measurable velocity $v_{\max}$ satisfies the following relationship:

$$v_{\max} = \frac{R\Delta x/4}{\Delta t} = \frac{R\Delta x/4f}{1000000}. \tag{4}$$

TABLE I. The summary of fan rotation speed range.

	Fan speed, ω (r/min)				
	1000	2000	3000	4000	5000
PIV	√	√	√	√	√
PIV (with glass particle)	√	√			
Hot-wire anemometer	√	√	√	√	√
CFD simulation	√				

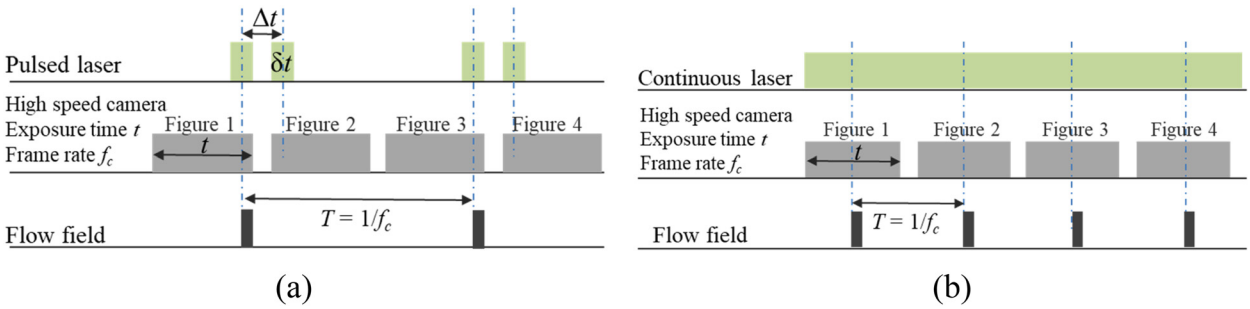

FIG. 2. Schematic diagram comparing the working modes of two high-frequency PIV systems. (a) High repetition rate pulsed laser; (b) continuous laser.

Here, R represents the spatial resolution, μm/pixel; Δx is the pixel size of the interrogation window, pixels; Δt is the inter-frame time, μs; f is the frame rate, Hz. The spatial area is approximately 40×40 mm^2. The key parameters are determined after extensive testing, as shown in Table II. The two-dimensional transient velocity field at a certain moment and the transient velocity series at the center point are illustrated in Fig. 3. It can be observed that the instantaneous velocity exhibits strong fluctuation characteristics.

The average velocities u_{ave} and v_{ave}, as well as the turbulent fluctuation velocities u_{rms} and v_{rms} at each point (x_i, y_i), are calculated as Eqs. (5) and (6). The scale of turbulent eddies is closely related to turbulent dissipation rate ε. Various methods can be used to calculate turbulent dissipation rate, including the velocity gradient method, structure function fitting method, large eddy PIV method, dimensional analysis, and energy spectrum curve fitting method.[37–39] The velocity gradient method is the most accurate method, requiring PIV measurements with high spatial resolution. The interrogation window Δx must satisfy $\eta/10 < \Delta x < \eta/2$ to accurately capture the velocity gradient, otherwise, the dissipation rate will be underestimated.[37,38] However, PIV measurements are essentially low-pass filtered and unable to provide sufficient spatial resolution to capture the smallest eddies that cause dissipation. The calculation methods using the 1D velocity gradient method, 2D velocity gradient method, energy spectrum curve fitting method, and dimensional analysis method are shown in Eqs. (7)–(10). The results are depicted in Fig. 4, showing that the velocity gradient method yields results significantly lower than the other two methods, while the dimensional analysis method and energy spectrum curve fitting method give consistent results

$$u_{ave}(x_i, y_i) = \frac{1}{N}\sum_{j=1}^{N} u(x_i, y_i),\ v_{ave}(x_i, y_i) = \frac{1}{N}\sum_{j=1}^{N} v(x_i, y_i), \tag{5}$$

$$\begin{aligned} u_{rms}(x_i, y_i) &= \sqrt{\frac{1}{N}\sum_{j=1}^{N}[u(x_i, y_i) - u_{ave}(x_i, y_i)]}, \\ v_{rms}(x_i, y_i) &= \sqrt{\frac{1}{N}\sum_{j=1}^{N}[v(x_i, y_i) - v_{ave}(x_i, y_i)]}, \end{aligned} \tag{6}$$

$$\varepsilon = 15\nu\left\langle\left(\frac{\partial u_1}{\partial x_1}\right)^2\right\rangle, \tag{7}$$

$$\varepsilon = \nu\left(2\left(\frac{\partial u}{\partial x}\right)^2 + 2\left(\frac{\partial v}{\partial y}\right)^2 + 3\left(\frac{\partial v}{\partial x}\right)^2 + 3\left(\frac{\partial u}{\partial y}\right)^2 + 2\frac{\partial u}{\partial y}\frac{\partial v}{\partial x}\right), \tag{8}$$

$$E_{11}(k_1) = C_1\varepsilon^{2/3}k_1^{-5/3}, \tag{9}$$

$$\varepsilon = A\frac{u_{\text{rms}}^3}{L}, \quad A = 0.85. \tag{10}$$

In this study, the dissipation rate ε is calculated using the dimensional analysis method, which is based on the Richardson–Kolmogorov energy cascade theory. It assumes that the turbulence is in a state of equilibrium, with the rate of turbulent kinetic energy transfer through large eddies being equal to the rate of transfer from large to small eddies. Therefore, the energy transfer rate can be characterized by the integral eddy scale L divided by the turbulent fluctuation velocity u_{rms}, and the energy transferred is the turbulent kinetic energy k.

TABLE II. Summary of the PIV measurement parameter.

	$\omega = 1000$ and 2000 r/min	$\omega = 3000$ and 4000 r/min	$\omega = 5000$ r/min
Frame rate, f	$f = 7039$ Hz	f = 14 615.6 Hz	f = 14 615.6 Hz
Exposure time, t	10 μs	10 μs	6.7 μs
Image resolution	1000×1000 pixels	600×600 pixels	600×600 pixels
Spatial resolution, R	$R = 41$ μm/pixel	R = 66.7 μm/pixel	R = 66.7 μm/pixel
Image number, N	$N = 48\,376$ (43.5 GB)	$N = 126\,291$ (20 GB)	$N = 126\,291$ (20 GB)
Flow time	6.87 s	8.64 s	8.64 s
Interrogation window, Δx	First $\Delta x = 64$ pixels, second $\Delta x = 32$ pixels, 50% overlap		
Maximum velocity, $v_{\max}$	4.62 m/s	15.60 m/s	15.60 m/s

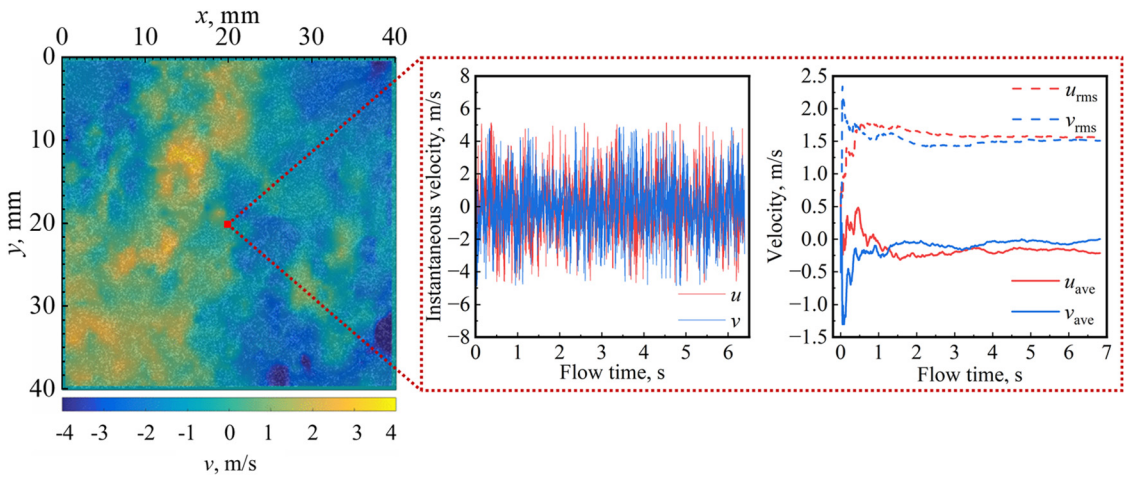

FIG. 3. Distribution of two-dimensional transient velocity field and temporal variation of transient velocity at the spatial center point when the fan speed is 2000 r/min.

This method requires the calculation of the integral eddy scale first. According to the relevant theories of turbulence,[13,23,40] spatial correlation coefficients R_{uu} and R_{vv}, longitudinal integral length L_{ux} and L_{vy}, and transverse integral length L_{uy} and L_{vx} are evaluated by Eqs. (11)–(13), respectively. Integral eddy length scale L is the average of L_{ux} and L_{vy}. The formula for calculating the turbulent kinetic energy k is given in Eq. (15). Turbulent Reynolds number Re_L and the integral timescale τ_L are defined in Eq. (16), where ν is the kinematic viscosity of air, taken as $14.8 \times 10^{-6}\,\mathrm{m^2/s}$. Taylor eddy length scale λ and its timescale τ_λ are given in Eq. (17). Kolmogorov eddy length scale η and the timescale τ_η are given in Eq. (18),

$$R_{uu}(\Delta x) = \frac{\langle u(x,y,t)u(x+\Delta x,y,t)\rangle}{u_{rms}^2}, \quad R_{vv}(\Delta y) = \frac{\langle v(x,y,t)v(x,y+\Delta y,t)\rangle}{v_{rms}^2}, \tag{11}$$

$$L_{ux} = \int_0^\infty R_{uu}(\Delta x,0)d(\Delta x), \quad L_{vy} = \int_0^\infty R_{vv}(\Delta y,0)d(\Delta y), \tag{12}$$

$$L_{uy} = \int_0^\infty R_{uu}(\Delta y,0)d(\Delta y), \quad L_{vx} = \int_0^\infty R_{vv}(\Delta x,0)d(\Delta x), \tag{13}$$

$$L = (L_{ux} + L_{vy})/2, \tag{14}$$

$$k = \frac{3}{2}\left(\frac{u_{rms}^2 + v_{rms}^2}{2}\right), \tag{15}$$

$$\mathrm{Re}_L = \frac{u_{rms}L}{\nu}, \quad \tau_L = \frac{L}{u_{rms}}, \tag{16}$$

$$\lambda = \left(\frac{15\nu u_{rms}^2}{\varepsilon}\right)^{\frac{1}{2}}, \quad \tau_\lambda = \frac{\lambda}{u_{rms}}, \tag{17}$$

$$\eta = \left(\frac{\nu^3}{\varepsilon}\right)^{\frac{1}{4}}, \quad \tau_\eta = \left(\frac{\nu}{\varepsilon}\right)^{\frac{1}{2}}. \tag{18}$$

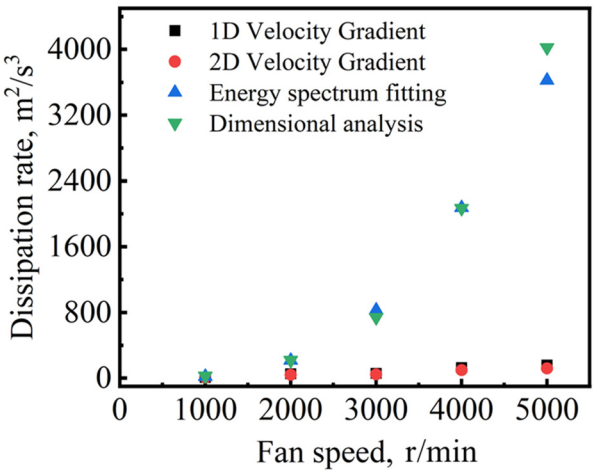

FIG. 4. Dissipation rate ε calculated by different methods.

C. Hot-wire anemometer measurement method

The hot-wire anemometer used in this study is Dantec MultiChannel CTA. The operation procedure is as follows. Initially, the measurement system was configured within the Streamware Pro software, setting the type of probe and support rod, ambient temperature, and connection line resistance. Subsequently, channel switches were activated in accordance with the software prompts. A two-point velocity calibrator was utilized to calibrate the speed–voltage curve of the selected probe while the directional angle coefficients were also calibrated for the three-dimensional probe. Finally, the probe was placed in the flow field to record the induced voltage and then obtain the velocity information through post-processing. Two types of probes were utilized, as shown in Fig. 5(a), which were 55R01 one-dimensional probe and 55R97 three-dimensional probe. 55R01 was only placed in the center of the furnace. For each fan speed, the probe was repositioned three times, allowing the hot wire to parallel to x, y, and z axes. 55R97 was situated at multiple points within the furnace, as indicated in Fig. 5(b), with a spatial distance of 10 mm between each point. The correspondence between the induced voltage and velocity is

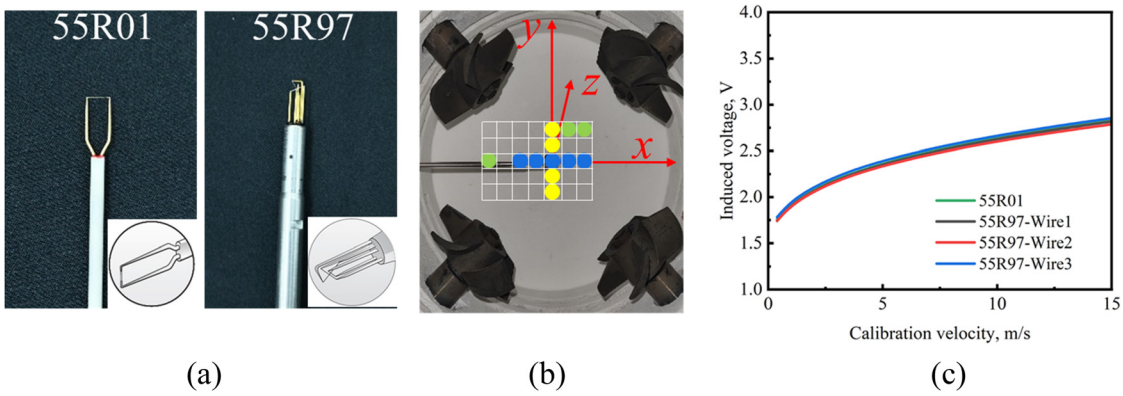

FIG. 5. Schematic diagram of hot-wire anemometer measurement. (a) The selected probes; (b) spatial location of the probes; (c) the correspondence between the induced voltage and velocity.

shown in Fig. 5(c). Since the two-point calibrator only provides low and high positions, corresponding to a velocity range of 1.59–49.59 m/s, the velocity–voltage calibration curve outside this range is obtained through extrapolation, which may not be accurate. When the actual flow field contains many velocities below 1.59 m/s, the velocity values obtained by HWA do not equate to the actual velocities in the flow field.

The sampling frequency was set at 30 kHz with each sampling duration being 60 s, resulting in approximately 1.8×10^6 data. Figure 6 illustrates the induced voltage and velocity of the 55R01 probe at a fan speed of 2000 r/min. It can be observed that both exhibit strong fluctuating characteristics, and the induced velocity has a minimum value of approximately 0.33 m/s, which is caused by the extrapolation in voltage–velocity calibration process. The mean and root mean square (RMS) of the instantaneous data series were analyzed. If the results obtained by the probes along different directions and spatial positions have consistent means and variances, it indicates that the actual velocity is uniform and isotropic.

D. Numerical simulation method

The geometric structure for the CFD simulation is shown in Fig. 7, consisting of four cylindrical rotating subdomains enclosing the fans and a larger stationary subdomain. The diameter of the rotating subdomains is 108 mm with a thickness of 45 mm. Due to the symmetric geometry, extensive preliminary simulations have shown that meshing only one-fourth of the geometry and then mapping it to the remaining three-fourths, with the interface for data exchange, can significantly improve the convergence. The poly-hexcore meshing method allows for sharing nodes between hexahedral and polyhedral meshes. The blade and furnace walls are set as no-slip and boundary layer meshes are added. The fluid within these cylindrical subdomains rotates at the same speed with the fans. The multiple reference frame (MRF) model in Fluent is employed to calculate the interaction between the rotating and stationary subdomains, which is a commonly used and efficient steady-state computational method. The pressure–velocity coupling is solved by the SIMPLE algorithm with a second-order differencing scheme.

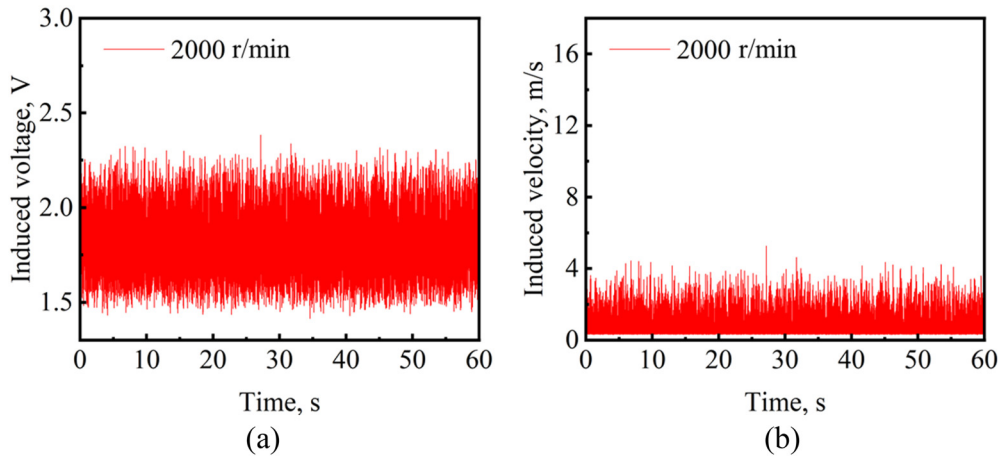

FIG. 6. Inducted voltage and cooling velocity of 55R01 placed along the *z* direction when the fans rotate at 2000 r/min. (a) Induced voltage; (b) induced velocity.

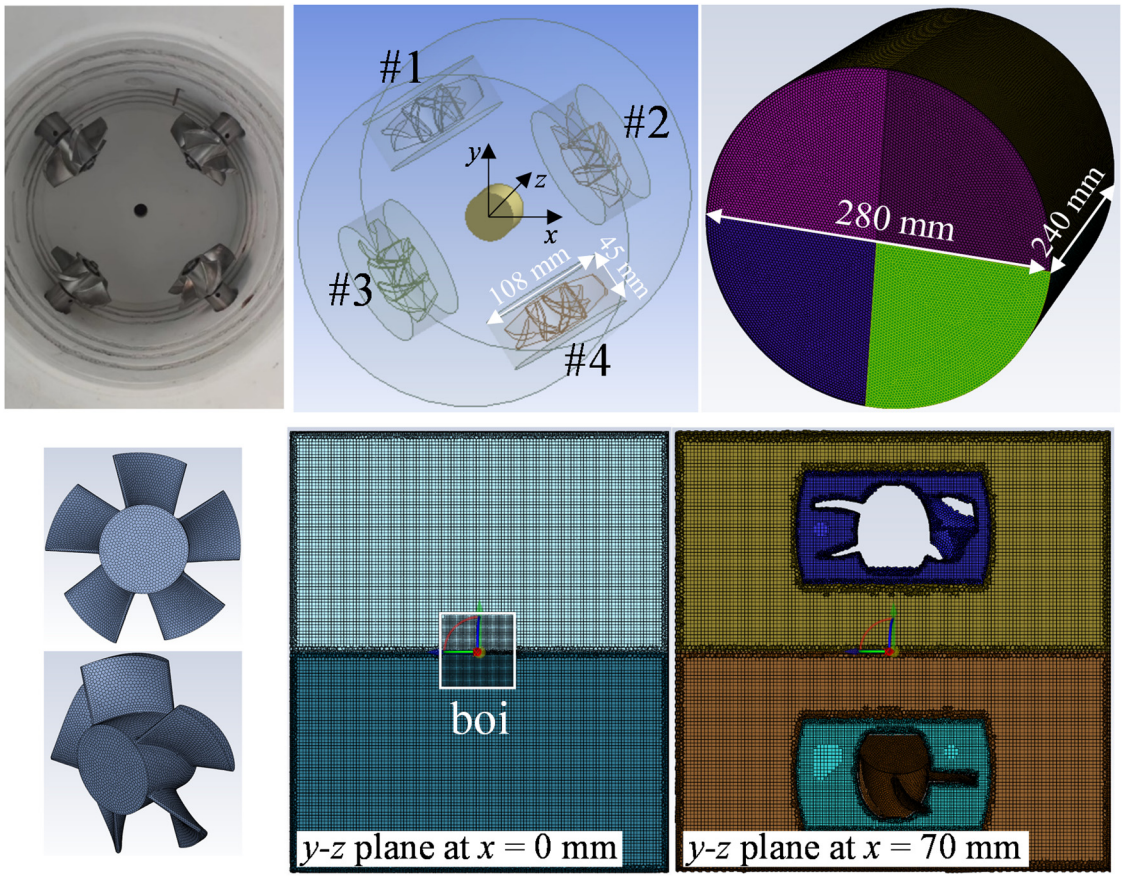

FIG. 7. Schematic diagram of the numerical simulation geometry structure and mesh division.

There are various turbulence models available for numerical simulations.[41,42] The k–ε model as a two-equation model offers simpler formulation and lower computational cost with reduced sensitivity to grid quality and initial conditions. This ensures better robustness and convergence in complex turbulent flow. Compared with the standard k–ε model, the realizable k–ε model improves the predictive ability of rotating mechanical flows by dynamically adjusting turbulent viscosity and is the preferred two-equation model for complex flow simulations.[43] Additionally, the k–ε model relies on the isotropic eddy viscosity assumption, which aligns with the observed flow characteristics in the central region of the device and potentially has higher accuracy, considering that the central flow features are of greater interest because subsequent experiments are conducted in this region. RSM accounts for streamline curvature, rotation, and rapid changes in strain rate to reflect the anisotropic of turbulence, making it suitable for simulating complex flow fields like high-speed swirling flows. However, the increased equations and convergence difficulties of RSM can significantly prolong computation times. The flow field generated by multiple fans is nearly isotropic in the central region but highly turbulent overall, making it difficult to assess the applicability of the two models. Consequently, both models have been employed in the literature.[31] The choice of turbulence model affects the accuracy of the solution. Therefore, both the realizable k–ε model and RSM are used and compared with PIV results.

A grid independence analysis is conducted using a coarse grid ($N = 1\,692\,444$) and a refined grid ($N = 3\,354\,956$) with both the realizable k–ε model and RSM model. The results in Fig. 8 demonstrate that k–ε model predictions achieves grid independence with fewer elements $N = 1\,692\,444$, whereas RSM predictions are more sensitive to grid number and discrepancies still persist even at $N = 3\,354\,956$. Balancing computational cost and accuracy, the refined grid $N = 3\,354\,956$ is selected. The mesh size in the central body of influence (BOI) region is 1 mm, in the rotating subdomains it ranges from 1 to 2 mm, and in the stationary subdomain from 1 to 4 mm, all with orthogonality quality greater than 0.5. Each case is iterated for approximately 100 000 steps, taking about 60 h on a 64-core computing center.

III. RESULTS AND DISCUSSION

A. Analysis of HWA, high-frequency PIV, and numerical simulation methods

Given the limited research on the application of HWA, high-frequency PIV, and steady-state simulation to the flow field of such

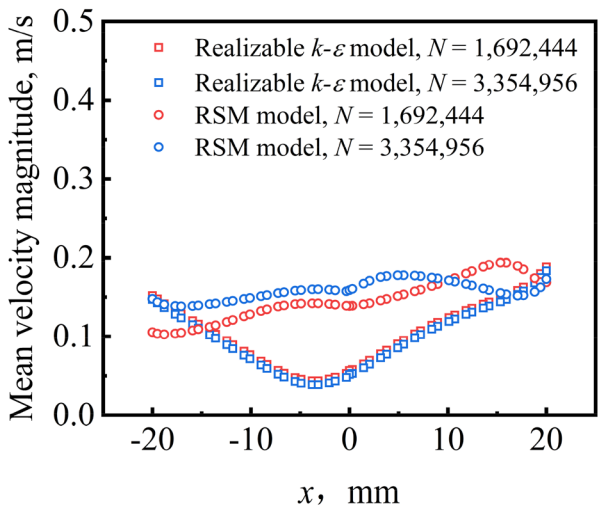

FIG. 8. Grid independence analysis using a coarse grid and a refined grid.

devices, this study first evaluates the applicability of these methods. The directional sensitivity of hot wire is initially examined. Figure 9 shows the induced voltage and velocity of the one-dimensional probe 55R01 placed along different orientations. The exit velocity of calibrator is 1.59 m/s. It can be observed that the cooling effect of the airflow on the hot wire varies when the wire is oriented parallel to the *x*, *y*, *z*, and *yz* diagonal directions, resulting in different induced voltages and velocities. The true velocity can only be accurately reflected when the hot wire is oriented along the *x* or *z* direction for 55R01. Three-dimensional probe 55R97 has the similar response. This indicates that if the induced results differ when the probe is placed in different orientations or positions, the flow exhibits a mean flow; otherwise, it is isotropic. This approach can be used to rapidly verify whether the flow at different locations meets homogeneous and isotropic characteristics.

Using continuous lasers combined with high-speed cameras for high-frequency PIV is currently rare, primarily because the frame interval Δt reaches tens of microseconds, which is the reciprocal of the frame rate f. As shown in Fig. 2, even with $f = 10\,000$ Hz, the frame interval is 100 μs, significantly larger than the interval in pulsed PIV. Under high-velocity flow conditions, this large frame interval leads to reduced correlation of image pairs, thereby compromising velocity accuracy. To analyze whether this high-frequency PIV can capture the transient flow at different fan speeds, Fig. 10 examines the consecutive frames and processed velocity fields with setting parameters listed in Table II. It can be observed that at 1000 and 3000 r/min, the differences between consecutive frames are minimal, indicating low flow velocities. The instantaneous velocity is far below v_{max} and eddy structures are clear, confirming the accuracy of the velocity measurements.

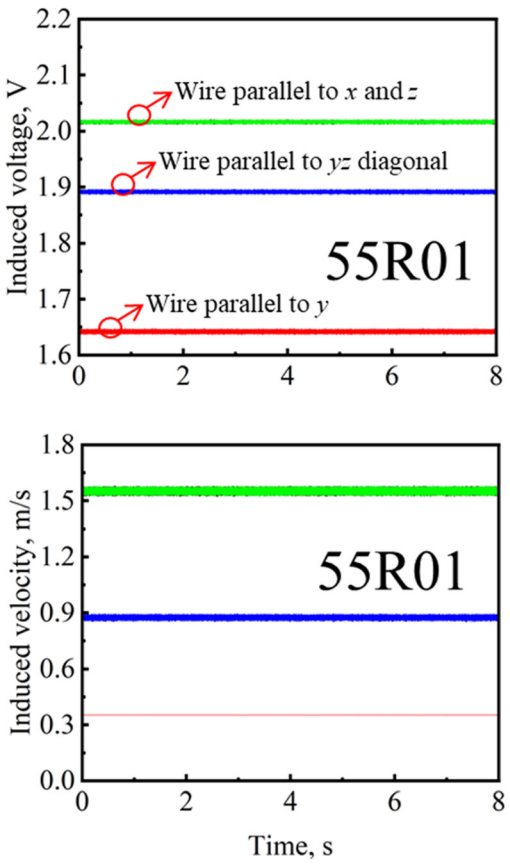

FIG. 9. Induced voltage and velocity of 55R01 placed along different directions in the same flow.

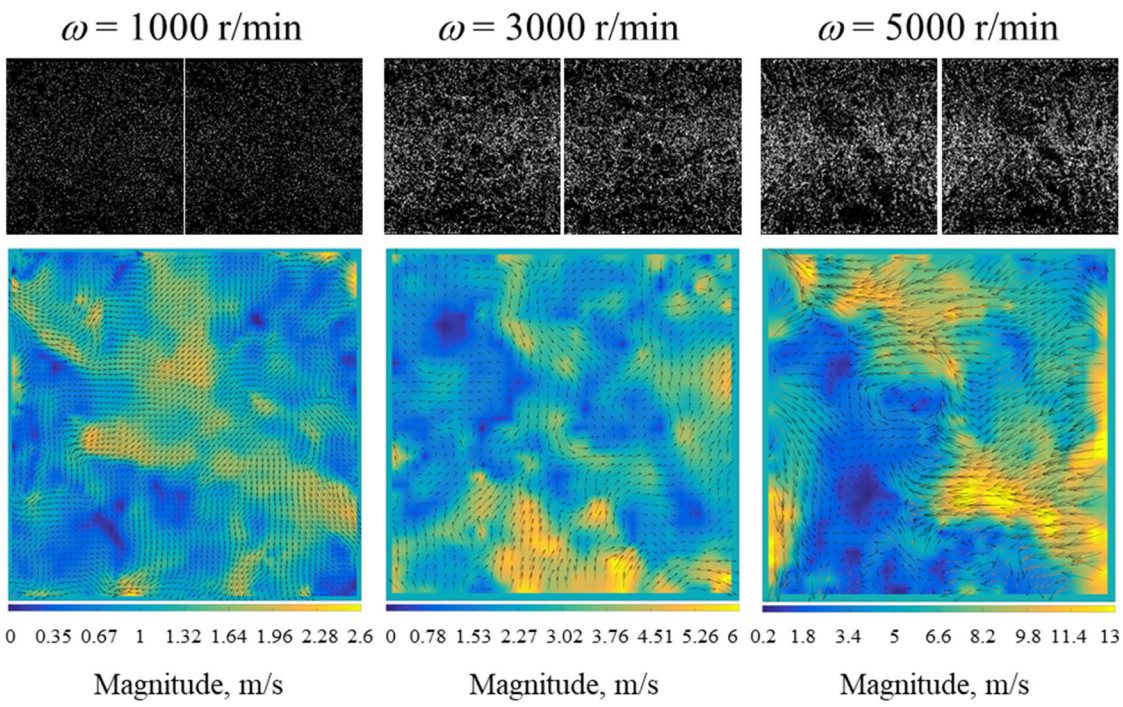

FIG. 10. Transient particle image pairs and velocity field obtained by PIV at different fan speeds.

Slight differences appear between consecutive frames at 5000 r/min, with the tracer particle distribution becoming non-uniform. The instantaneous maximum velocity approaches v_{max}, resulting in a slight decrease in analysis accuracy. Overall, the measurement parameters listed in Table II meet the requirements. It should be noted that to increase the frame rate at high fan speeds, the image size is reduced from 1000 × 1000 to 600 × 600 pixels, resulting in the spatial resolution R increases from 41 to 66.7 μm/pixel. In fact, finer spatial resolution is needed due to the reduction in eddy scales at high fan speeds, which would narrow the view field. This indicates that this method is not suitable for flow measurements with high velocities and large view field.

Steady-state simulation using the realizable k–ε model and RSM reveals that the former converges after approximately 100 000 iterations, while the latter requires nearly 200 000 iterations to stabilize but minor oscillations still present. The reason is that RSM model directly solves the individual components of the Reynolds stress instead of assuming isotropic eddy viscosity, requiring solving seven transport equations in three-dimensional simulation, which are highly nonlinear and coupled. This inherent complexity greatly increases the convergence difficulty. In addition, in the central region where the flow exhibits isotropic behavior, the RSM predictions by physically rigorous formulation is highly sensitive to mesh quality and pressure fluctuation. Minor mesh irregularities or pressure–velocity decoupling can

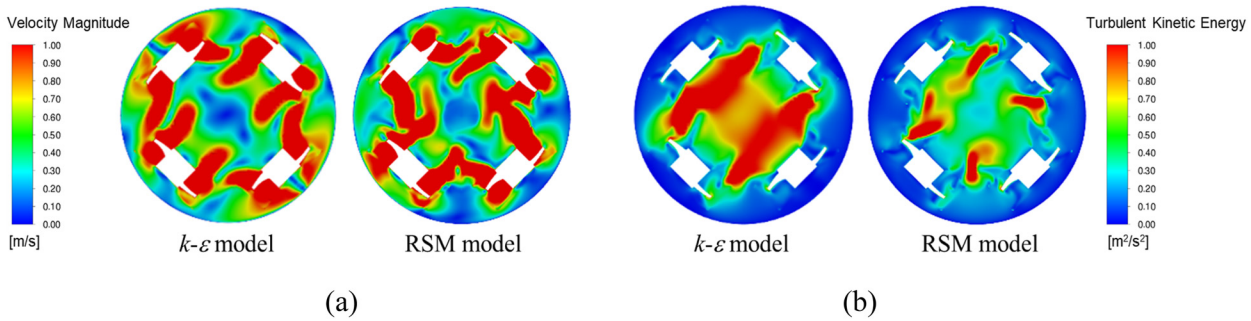

FIG. 11. Comparison of the realizable k–ε model and RSM model at $\omega = 1000$ r/min. (a) Mean velocity magnitude; (b) turbulent kinetic energy k.

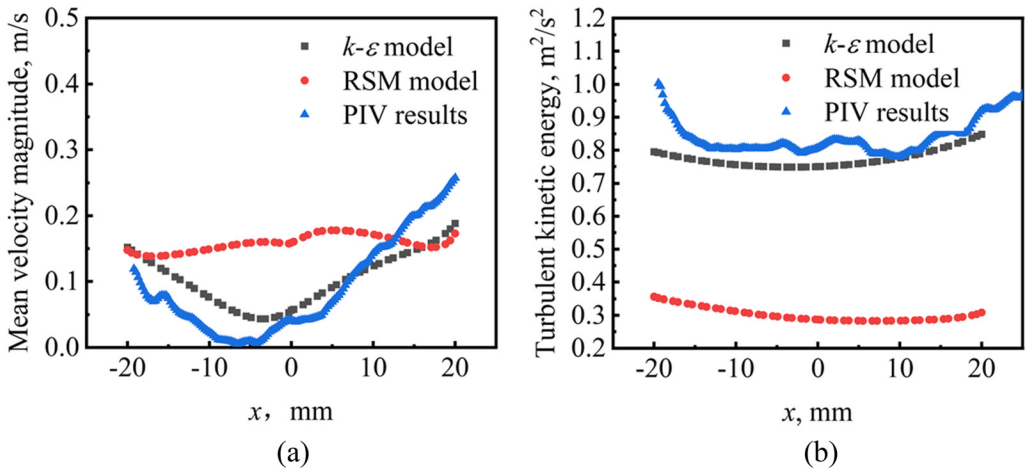

FIG. 12. Comparison of the realizable k–ε model and RSM model with PIV results at the central zone when $\omega = 1000$ r/min. (a) Mean velocity magnitude; (b) turbulent kinetic energy.

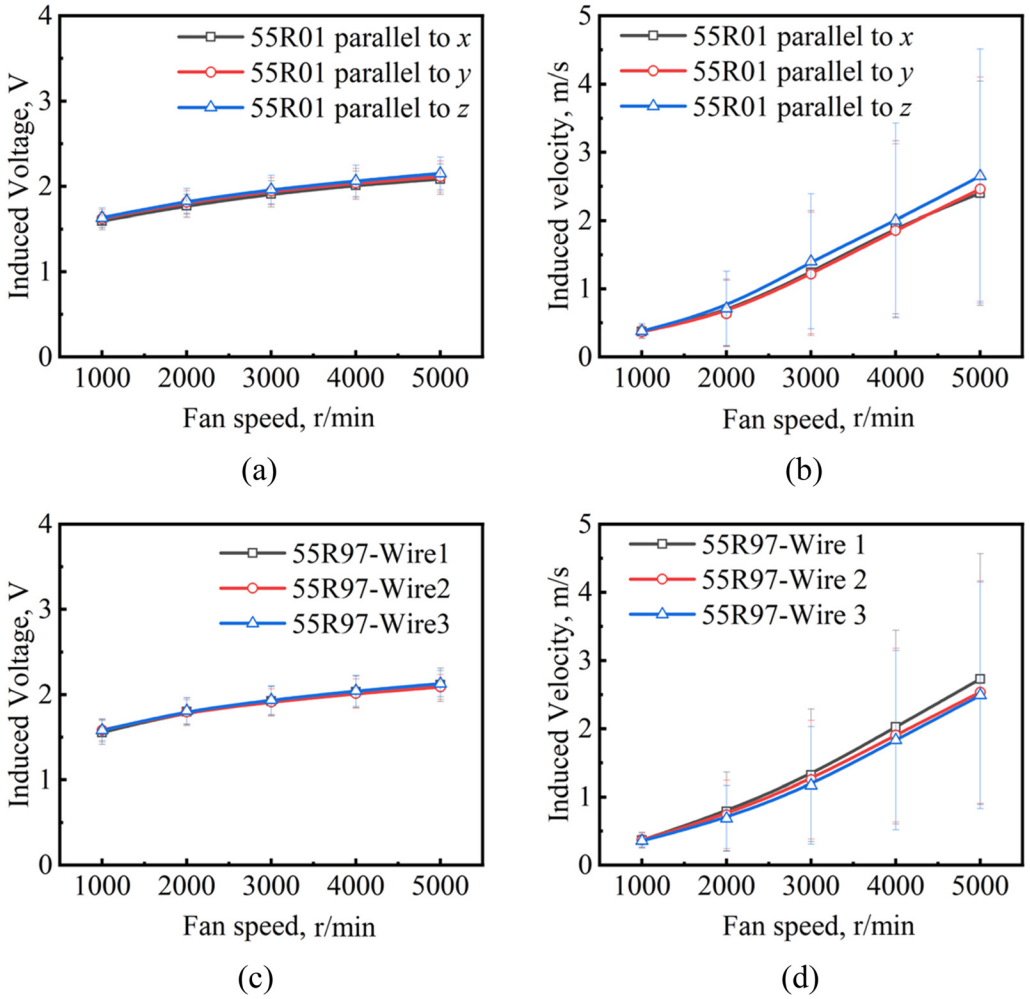

FIG. 13. Induced voltage and velocity of 55R01 and 55R97 at the furnace center point.

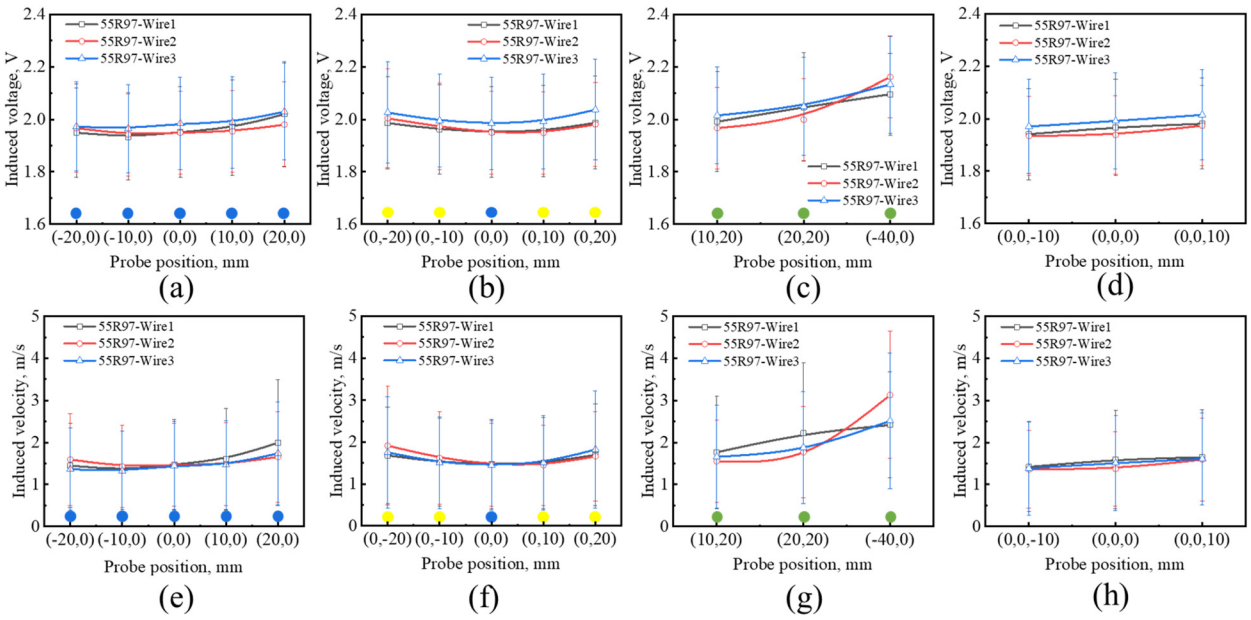

FIG. 14. Induced voltage and velocity of 55R97 at different positions when $\omega = 3000$ r/min.

propagate through the tightly coupled stress equations, leading to numerical instability. Consequently, the monitored velocity in this region fluctuates slightly around 0 m/s. Distributions of mean velocity and turbulent kinetic energy in the x–y plane at $z = 0$ when $\omega = 1000$ r/min are shown in Fig. 11, which indicates that the flow field calculated by k–ε model is more regular and smooth, whereas the RSM model yields a more turbulent structure. Comparing these model predictions with PIV results in the central region over 40 mm along the x axis, as shown in Fig. 12, it is found that the k–ε model more closely aligns with PIV results. Although the RSM model captures more detailed flow structures, the computed turbulent kinetic energy is significantly lower than PIV results. This indicates that in steady calculation, with the same grid quality and computing resources, the k–ε model provides more accurate predictions for isotropic turbulence, which is also confirmed by some studies.[44]

B. Flow characteristics in the furnace central region

HWA can preliminarily determine the spatial range that meets the HIT characteristics in the furnace. Figure 13 shows the induced voltage and velocity of one-dimensional probe 55R01 placed along different directions and three-dimensional probe 55R97 at the furnace center point (0, 0, and 0 mm). It can be seen that under the same fan speed, the hot wires in different directions sense almost the same voltage and velocity, that is, the flow field has the same cooling effect on the different hot wires, which indicates the flow isotropy at this location. Furthermore, the fan speed was set at 3000 r/min, and 55R97 was placed at multiple positions [shown in Fig. 5(b)] using a 3D mobile platform. The induced voltage and velocity are shown in Fig. 14. It can be seen that in the central spherical area with a radius of $r = 10$ mm, as shown in Figs. 14(a)–14(b), 14(e)–14(f), and 14(d)–14(h), the response of different hot wires is consistent, and the flow field strictly meets the HIT characteristics. The central spherical area with $r = 20$ mm also basically satisfies. However, as shown in Figs. 14(c)–14(g), the response of different hot wires is different in the spherical area with $r > 20$ mm, indicating the flow field departs from the HIT characteristics.

The HWA analysis quickly confirmed that the flow field within a central radius of $r = 20$ mm essentially meets the criteria for HIT. Therefore, the PIV field of view is also confined to this spatial range. Figure 15 summarizes the PIV measurement results under different fan speeds, including the mean velocity u_{ave} and v_{ave}, and the fluctuating velocity u_{rms} and v_{rms}. It can be observed that a small mean flow exists at the periphery of the field of view, especially at high fan speed. In the central region, only turbulent fluctuation velocities are present and the velocity components u_{rms} and v_{rms} are very close, while the mean velocities approaching to 0 m/s. Statistically, the turbulent fluctuating velocity has an almost linear relationship with the fan speed, $u_{rms} = 0.000\,814\,\omega$ (r/min), as shown in Fig. 16.

In turbulent flows, large eddies carry energy and transfer it to smaller eddies through a cascade process, where the energy is eventually dissipated. To further elucidate the spatiotemporal scales of eddies with different sizes, cross correlation analysis of velocity fields were conducted. As shown in Figs. 17(a) and 17(b), taking $\omega = 1000$ r/min as an example, the spatial correlation coefficient distribution is obtained by cross-correlating the spatial velocity with that at the center point. The R_{uu} profile along the x axis and R_{vv} along the y axis are extrapolated and integrated to determine the longitudinal integral length scale, as shown in Fig. 17(c). The R_{uu} profile along the y axis and R_{vv} along the x axis are integrated to obtain the transverse integral length scale, as shown in Fig. 17(d). The eddy scales calculated by Eqs. (12)–(18) are summarized in Fig. 18. It can be observed from Fig. 18(a) that integral length

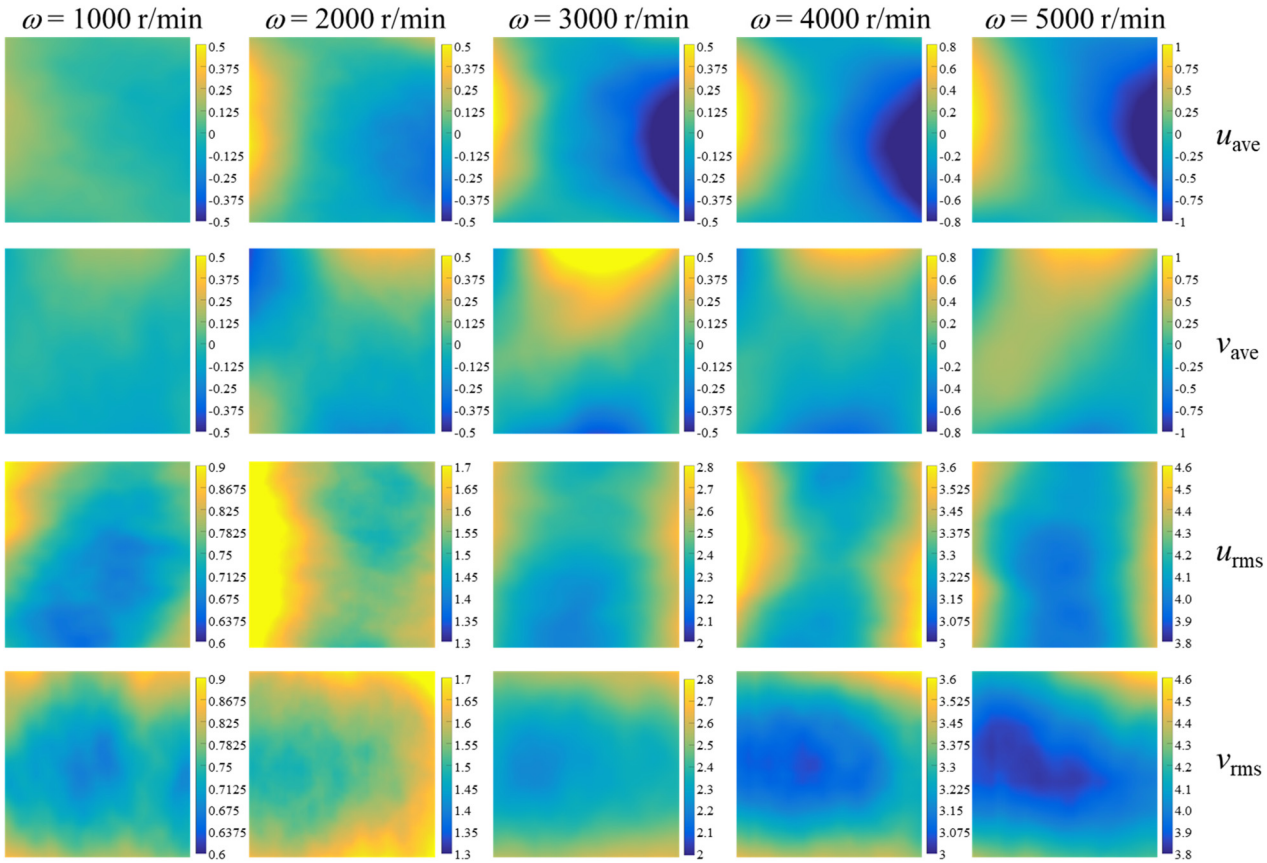

FIG. 15. Spatial distribution of mean velocity and turbulent fluctuation velocity at different fan speeds.

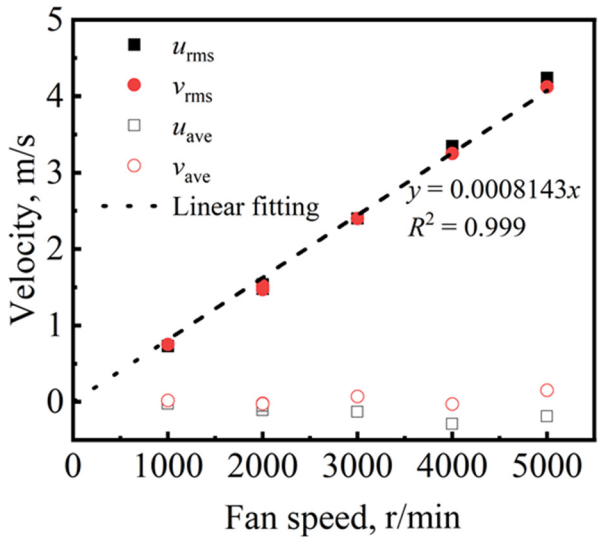

FIG. 16. Mean velocity and turbulent fluctuation velocity at different fan speeds.

increases slightly with fan speed. Longitudinal integral length (L_{ux} and L_{vy}) stabilize within 13–16 mm, while the transverse length (L_{uy} and L_{vx}) maintain around 7.3–8 mm, aligning with the statistical theory of homogeneous turbulence that transverse length equals to half of the longitudinal length.[45] Temporal and spatial scales of Taylor eddy λ and Kolmogorov eddy η both decrease significantly with increasing ω, while the Reynolds number increases markedly from Figs. 18(c) and 18(d).

Spectral analysis can reveal the distribution of turbulent energy.[46] High-frequency PIV measurements capture the continuous and transient changes in the flow field, and the calculated energy spectrum curves are shown in Fig. 19. It can be observed that there is no obvious energy-containing range within the PIV field of view and the spectrum is primarily composed of an inertial subrange and a dissipation range. The inertial subrange follows Kolmogorov's −5/3 scaling law, which clearly indicates that the flow field exhibits the typical HIT characteristics As the fan speed increases, the energy spectrum curve shifts upward, implying that higher fan speeds result in higher energy carried by the same scale eddies. It should be noted that the range of wavenumbers resolved by PIV is related to the spatial resolution R. Increasing the fan speed reduces the spatial resolution,

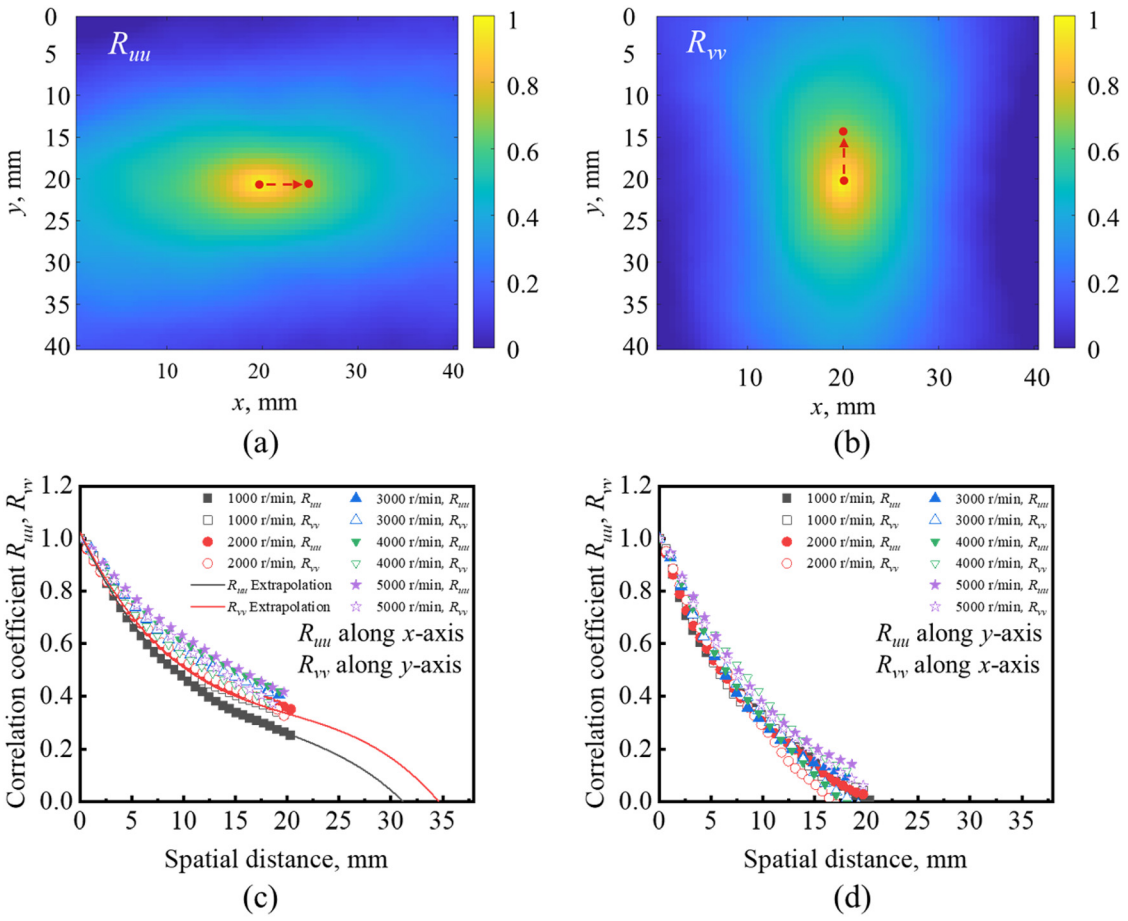

FIG. 17. Velocity correlation distribution. (a) R_{uu}; (b) R_{vv}; (c) longitudinal correlation; (d) transverse correlation.

thereby decreasing the maximum resolvable wavenumber (i.e., the smallest eddy size), as shown in Fig. 19(a). However, the energy spectrum calculated by a single-point high-frequency velocity is not affected by this limitation, as shown in Fig. 19(b). The frequency spectrum in Fig. 20(a) shows that the transient velocities have high energy at low frequencies and low energy at high frequencies, and no peak appears at the fan rotation frequency, indicating that the periodic blade rotation has no effect on the flow characteristics. The PDF distribution of instantaneous velocity in Fig. 20(b) is highly consistent with the standard Gaussian distribution.

C. Flow characteristics around a solid glass bead

After characterizing the flow field using high-frequency PIV, a 4 mm glass bead is fixed at the furnace center, and PIV measurements are conducted again to compare the impact of implanting particle on the turbulent characteristics. At 1000 r/min, $d/\eta = 40$ and $d/\lambda = 1.9$ while $d/\eta = 65$ and $d/\lambda = 2.5$ at 2000 r/min. The glass bead used in the experiment is made of K9 optical glass, which has good optical transmissivity and low reflectivity, allowing the laser to pass through and clear visualization of the boundary flow around the particle. The tracer particle image with the glass bead is shown in Fig. 21, where the particle boundary can be clearly seen. A mask is created on the glass bead to exclude it from the calculation during post-processing in PIVlab.

Comparing the flow fields with and without the presence of a large glass bead in Fig. 22 reveals that the glass particle induces a rebound effect on the mean velocity around it, as indicated by the red arrows in Fig. 22(a). The turbulent fluctuation velocities u_{rms} and v_{rms} near the particle are gradually reduced in Fig. 22(b), indicating the phenomenon of turbulent attenuation. For regions far from the glass particle, the flow field remains essentially the same as in the case without the particle. Furthermore, comparisons of the turbulent fluctuation velocity magnitude along the x and y axes are shown in Fig. 23. It can be observed that the thickness of the velocity boundary layer near the particle is approximately equal to its radius 2 mm, as marked in the dotted line in Fig. 23(b). When the fan speed increases from 1000 to 2000 r/min, the thickness of the particle velocity boundary layer decreases due to the turbulent level increases, which is consistent with expectations.

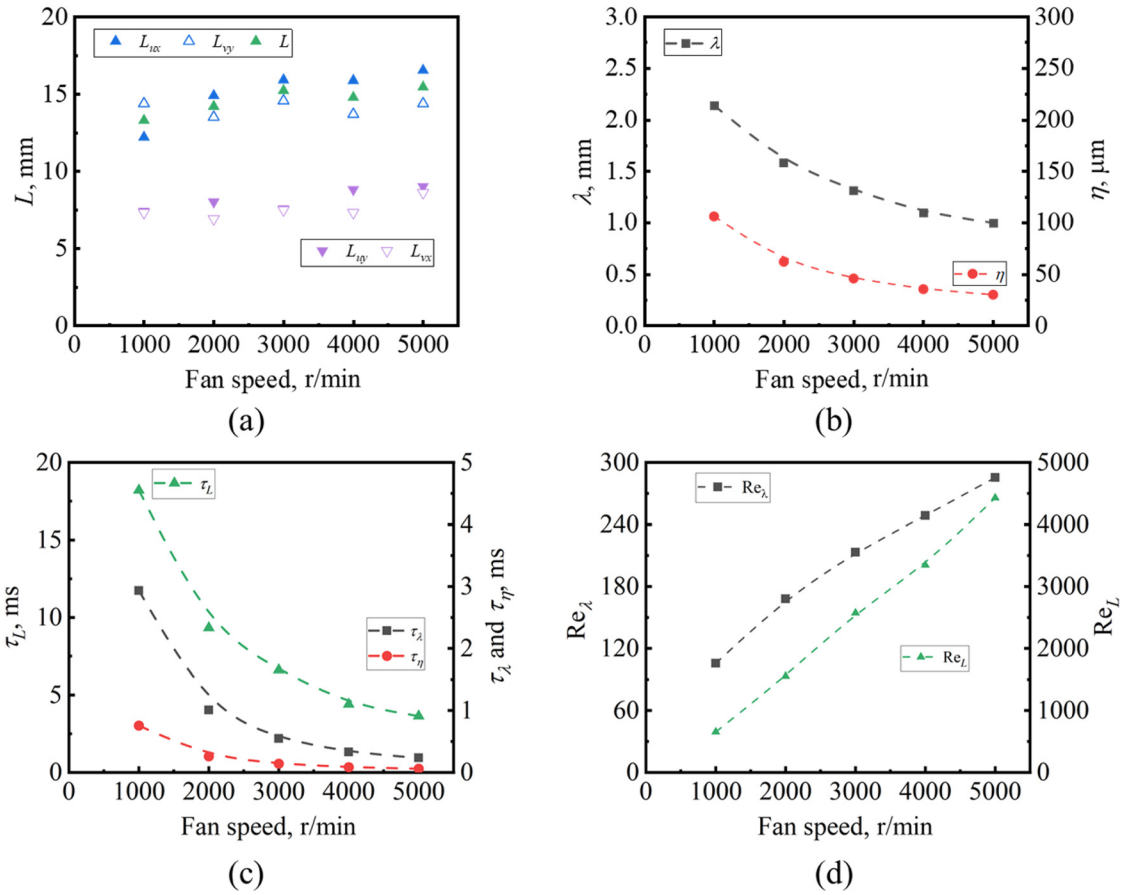

FIG. 18. Measured eddy characteristics. (a) Longitudinal and transverse integral scale; (b) Taylor scale and Kolmogorov scale; (c) spatial scale; (d) integral Reynolds number Re_L and Taylor Reynolds number Re_λ.

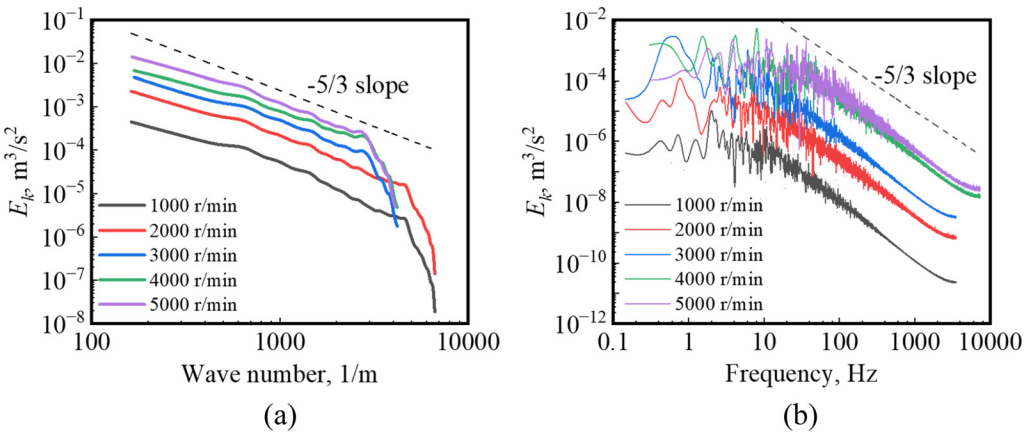

FIG. 19. Energy spectrum of PIV flow field at different fan speeds. (a) Calculated based on transient velocity field; (b) calculated based on single-point high-frequency velocity sequence.

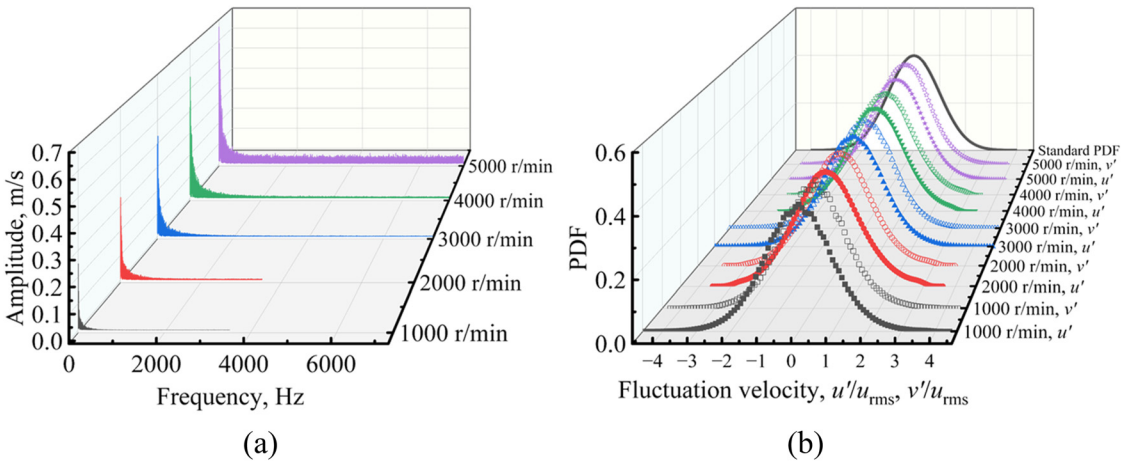

FIG. 20. Frequency spectrum and PDF distribution of PIV flow field at different fan speeds. (a) Frequency spectrum; (b) PDF distribution.

D. Flow characteristics in the furnace entire region

HWA and PIV measurements can only provide limited flow field information in the furnace central region. The flow characteristics outside the central region in the four-fan opposed furnace require simulation analysis. In Sec. III A, the rationality of using the realizable k–ε turbulence model combined with MRF for steady-state calculations has been demonstrated. As shown in Fig. 11, the HIT in the central region is formed by the opposed impingement of airflow generated by the rotational fans, with the highest mean velocity in the fan rotation region, gradually decreasing toward the center. Unlike some transient simulation research works[29,30] that show the highest turbulent kinetic energy in the fan regions, the present study reveals that the highest turbulent kinetic energy k is located at the intersection of the flows from adjacent fans, and then the central region. Figure 24 shows the distribution of mean velocity and turbulent kinetic energy in the y–z plane at $x = 0$. It is found that despite the four fans being arranged in the x–y plane, in the central region within a 30 mm range, the mean velocity is close to 0 m/s and the turbulence kinetic energy is consistent with that in the x–y plane shown in Fig. 11, indicating that a limited number of large size fans can create a three-dimensional flow in the central region that meets the characteristics of HIT.

IV. CONCLUSIONS

This research conducted a detailed experimental and numerical analysis of turbulence flow characteristics in a four-fan opposed combustion furnace. This study validated the use of HWA for rapid isotropy assessment and high-frequency PIV for accurately capturing continuous eddy motion. Within a 40 mm central region, the flow field exhibited HIT characteristics, with turbulent fluctuation velocity linearly related to fan speed, $u_{rms} = 0.000\,814\ \omega$. Integral eddy length

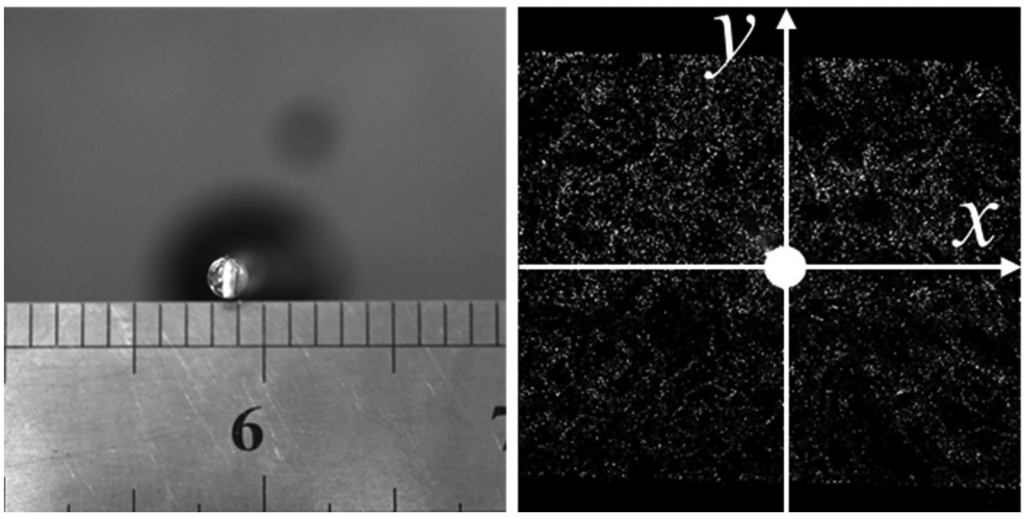

FIG. 21. The implantation of a 4 mm glass bead in the furnace center and the created mask in the PIV post-process.

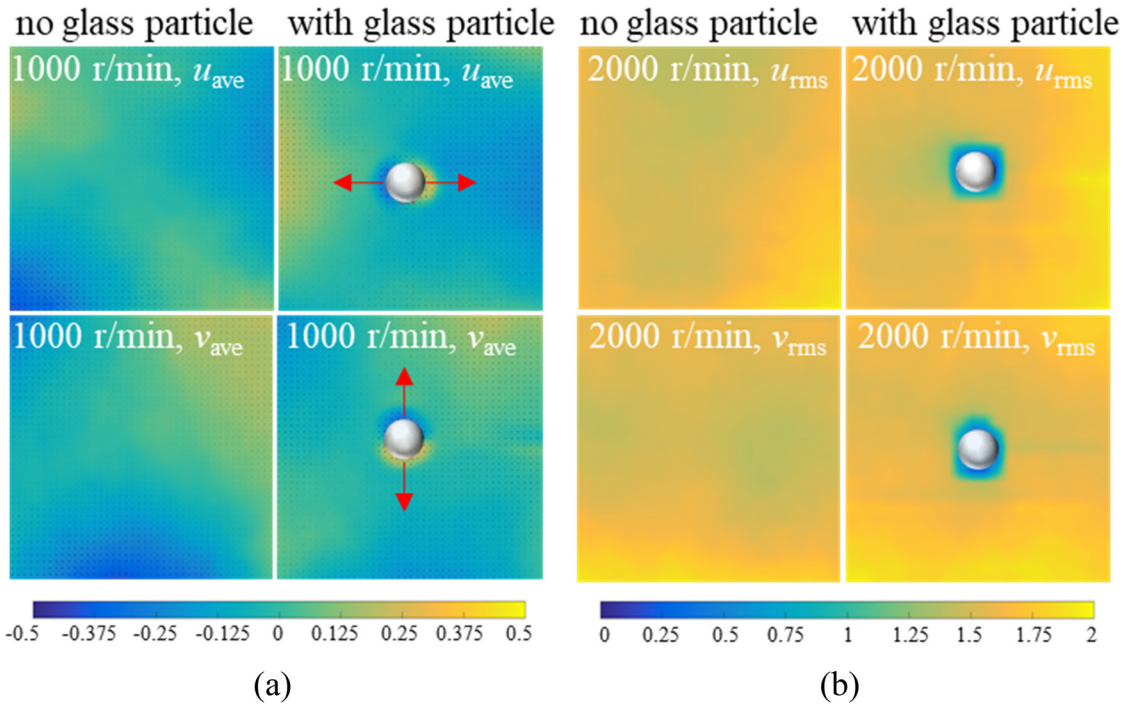

FIG. 22. The comparison of flow characteristics with a glass bead located in the central zone. (a) Mean velocity; (b) turbulent fluctuation velocity.

remains around 14 mm, while Taylor and Kolmogorov eddy length decreases with higher fan speeds, indicating enhanced turbulence intensity. The steady simulation using the realizable k–ε model and MRF method can accurately capture the flow field. Simulation results provide detailed insight into the broader flow characteristics, showing that turbulence kinetic energy peaks at the intersection of adjacent fan flows, and decreases toward the center. Despite the planar fan arrangement, three-dimensional HIT properties are formed in the central region. Furthermore, implanting a solid spherical glass particle in the HIT region reveals a localized reduction in turbulence intensity near the particle due to wall attenuation, while the flow far from the glass particle is unaffected. This result emphasizes that the boundary layer

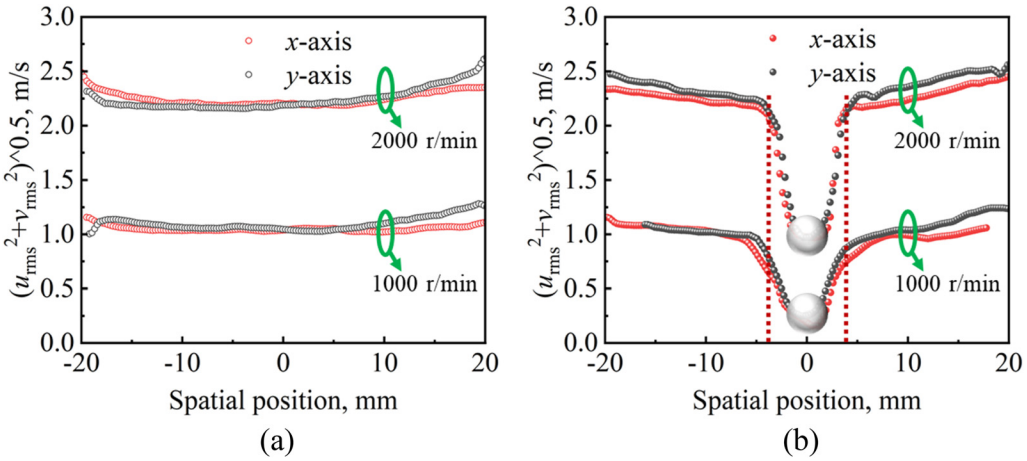

FIG. 23. The comparison of turbulent fluctuation velocity magnitude in the x–y plane with and without a glass bead located in the central zone. (a) Without a glass bead; (b) with a 4 mm spherical glass bead.

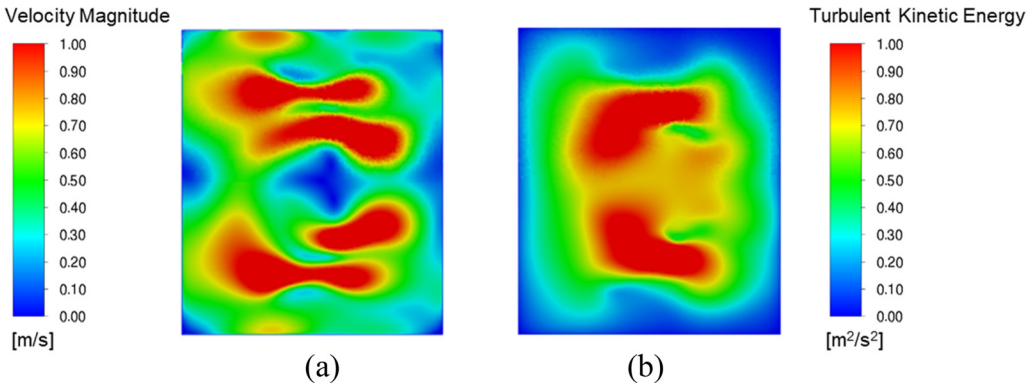

FIG. 24. The flow field distribution on the y–z plane at $x = 0$. (a) Mean velocity magnitude; (b) turbulent kinetic energy k.

thickness decreases at higher fan speeds and placing such particles has only a minimal effect on the overall flow field.

ACKNOWLEDGMENTS

This work was supported by the Carbon Neutrality and Energy System Transformation program (CNEST) led by Tsinghua University, Science and Technology Plan Project of Yunnan Province (202302AQ370003-2), Huaneng Group Science and Technology Research Project (HNKJ23-H71-U23GCZH03), and the Fundamental Research Funds for the Central Universities (2022ZFJH004).

AUTHOR DECLARATIONS

Conflict of Interest

The authors have no conflicts to disclose.

Author Contributions

Huina Guo: Conceptualization (equal); Data curation (equal); Investigation (equal); Methodology (equal); Writing – original draft (equal). **Xinde Zhang:** Writing – original draft (equal). **Zhoutao Cen:** Methodology (equal). **Xin Li:** Methodology (equal). **Yuxin Wu:** Conceptualization (equal); Funding acquisition (equal); Supervision (equal); Writing – review & editing (equal).

DATA AVAILABILITY

The data that support the findings of this study are available from the corresponding author upon reasonable request.

REFERENCES

[1]J. Goulier, N. Chaumeix, F. Halter, N. Meynet, and A. Bentaïb, "Experimental study of laminar and turbulent flame speed of a spherical flame in a fan-stirred closed vessel for hydrogen safety application," Nucl. Eng. Des. **312**, 214–227 (2017).
[2]Z. Y. Sun and C. Xu, "Turbulent burning velocity of stoichiometric syngas flames with different hydrogen volumetric fractions upon constant-volume method with multi-zone model," Int. J. Hydrogen Energy **45**(7), 4969–4978 (2020).
[3]C. Verwey and M. Birouk, "An experimental assessment of the enhancement of fuel droplet vaporization in a very high turbulence intensity environment," Proc. Combust. Inst. **38**(2), 3243–3250 (2021).
[4]C. Verwey and M. Birouk, "Fuel vaporization: Effect of droplet size and turbulence at elevated temperature and pressure," Combust. Flame **189**, 33–45 (2018).
[5]H. Lian, X. Y. Chang, and Y. Hardalupas, "Time resolved measurements of droplet preferential concentration in homogeneous isotropic turbulence without mean flow," Phys. Fluids **31**(2), 025103 (2019).
[6]M. Birouk, C. Chauveau, and I. Gökalp, "Turbulence effects on the combustion of single hydrocarbon droplets," Proc. Combust. Inst. **28**(1), 1015–1021 (2000).
[7]M. Birouk and S. L. Toth, "Vaporization and combustion of a soybean biodiesel droplet in turbulent environment at elevated ambient pressure," Combust. Sci. Technol. **187**(6), 937–952 (2015).
[8]H. Guo, Y. Wu, J. Liu, L. Feng, and H. Zhang, "Effects of turbulent mixing on structural evolution and combustion characteristics of woody biomass particles," Chem. Eng. J. **503**, 158680 (2025).
[9]Y. Xia, N. Hashimoto, and O. Fujita, "Turbulent flame propagation limits in polymethylmethacrylate particle cloud combustion," Proc. Combust. Inst. **40**(1), 105511 (2024).
[10]K. Hadi, R. Ichimura, N. Hashimoto, and O. Fujita, "Spherical turbulent flame propagation of pulverized coal particle clouds in an O_2/N_2 atmosphere," Proc. Combust. Inst. **37**(3), 2935–2942 (2019).
[11]J. Krüger, N. E. L. Haugen, and T. Løvås, "Correlation effects between turbulence and the conversion rate of pulverized char particles," Combust. Flame **185**, 160–172 (2017).
[12]W. Hwang, *Modification of Homogeneous and Isotropic Turbulence by Solid Particles* (Stanford University, Ann Arbor, 2005), p. 197.
[13]Z. Dou, Z. K. Pecenak, L. Cao, S. H. Woodward, Z. Liang, and H. Meng, "PIV measurement of high-Reynolds-number homogeneous and isotropic turbulence in an enclosed flow apparatus with fan agitation," Meas. Sci. Technol. **27**(3), 035305 (2016).
[14]Y. Wu, H. Guo, Z. Hu, and S. Zhang, "Heat transfer and ignition characteristics of millimeter-scale particles in turbulent flow field," J. China Coal Soc. **47**(1), 489–498 (2022).
[15]Y. Lin and X. Haitao, "Experimental investigation of pressure statistics in laboratory homogeneous isotropic turbulence," Phys. Fluids **35**(6), 065129 (2023).
[16]H. Zhu, C. Pan, and H. Lian, "Spatial correlations and relative velocities of polydisperse droplets in homogeneous isotropic turbulence," Phys. Fluids **34**(8), 083320 (2022).
[17]G. Huang, X. Lv, W. Chen, Y. Song, J. Yin, and D. Wang, "Generation of nearly homogeneous isotropic turbulence using a novel oscillating grid system," Phys. Fluids **36**(3), 035129 (2024).
[18]Q. Li and N.-S. Cheng, "Experimental investigation of characteristics of turbulence induced by multiple oscillating grids," Phys. Fluids **36**(3), 035140 (2024).
[19]E. S. Semenov, "Measurement of turbulence characteristics in a closed volume with artificial turbulence," Combust. Explos. Shock Waves **1**(2), 57–62 (1965).
[20]S. Ravi, S. J. Peltier, and E. L. Petersen, "Analysis of the impact of impeller geometry on the turbulent statistics inside a fan-stirred, cylindrical flame speed vessel using PIV," Exp. Fluids **54**(1), 1–16 (2012).

[21]M. Nakahara and H. Kido, "Study on the turbulent burning velocity of hydrogen mixtures including hydrocarbon," AIAA J. **46**(7), 1569–1575 (2008).
[22]B. Leisenheimer and W. Leuckel, "Self-generated acceleration of confined deflagrative flame fronts," Combust. Sci. Technol. **118**(1–3), 147–164 (1996).
[23]L. Cao, *Experimental Study of Aerosol Clustering in Isotropic Turbulence by Holographic Imaging* (State University of New York at Buffalo, Ann Arbor, 2007), p. 110.
[24]H. Zhao, J. Wang, X. Cai, Z. Bian, H. Dai, and Z. Huang, "Development of a fan-stirred constant volume combustion chamber and turbulence measurement with PIV," Front. Energy **16**(6), 973–987 (2022).
[25]D. Bradley, M. Haq, R. Hicks, T. Kitagawa, M. Lawes, C. Sheppard, and R. Woolley, "Turbulent burning velocity, burned gas distribution, and associated flame surface definition," Combust. Flame **133**(4), 415–430 (2003).
[26]B. Galmiche, N. Mazellier, F. Halter, and F. Foucher, "Turbulence characterization of a high-pressure high-temperature fan-stirred combustion vessel using LDV, PIV and TR-PIV measurements," Exp. Fluids **55**(1), 1636 (2014).
[27]Q. Chen, *High-Frequency Measurement of Vortices in Open Channel Flow with Particle Image Velocimetry* (Tsinghua University, 2014).
[28]D. Ferraro, R. Gaudio, and S. Ferrari, "Laboratory study of orifice jets from a pressurized pipe," Phys. Fluids **37**(3), 035139 (2025).
[29]F. Zhang, T. Zirwes, P. Habisreuther, N. Zarzalis, H. Bockhorn, and D. Trimis, "Numerical computation of turbulent flow fields in a fan-stirred combustion bomb," Combust. Sci. Technol. **193**(4), 594–610 (2021).
[30]A. Bonhomme, F. Duchaine, G. Wang, L. Selle, and T. Poinsot, "A parallel multidomain strategy to compute turbulent flows in fan-stirred closed vessels," Comput. Fluids **101**, 183–193 (2014).
[31]M. E. Morsy and J. Yang, "Numerical and experimental study on turbulence statistics in a large fan-stirred combustion vessel," Exp. Fluids **62**(5), 116 (2021).
[32]C. Verwey and M. Birouk, "Modulation of forced isotropic turbulence by an anchored droplet with near-Kolmogorov diameter and varying volatility," J. Fluid Mech. **966**, A10 (2023).
[33]M. M. Hoque, S. Mitra, M. J. Sathe, J. B. Joshi, and G. M. Evans, "Experimental investigation on modulation of homogeneous and isotropic turbulence in the presence of single particle using time-resolved PIV," Chem. Eng. Sci. **153**, 308–329 (2016).
[34]O. A. Mannaa, M. S. Mansour, S. H. Chung, and W. L. Roberts, "Characterization of turbulence in an optically accessible fan-stirred spherical combustion chamber," Combust. Sci. Technol. **193**(7), 1231–1257 (2021).
[35]L. Feng, Y. Wu, H. Guo, Z. Hu, S. Zhang, and H. Zhou, "Effect of fluctuation on heat transfer enhancement of a spherical particle," Int. Commun. Heat Mass Transfer **133**, 105981 (2022).
[36]M. Samimy and S. K. Lele, "Motion of particles with inertia in a compressible free shear layer," Phys. Fluids A **3**(8), 1915–1923 (1991).
[37]G. Wang, F. Yang, K. Wu, Y. Ma, C. Peng, T. Liu, and L.-P. Wang, "Estimation of the dissipation rate of turbulent kinetic energy: A review," Chem. Eng. Sci. **229**, 116133 (2021).
[38]J. de Jong, L. Cao, S. H. Woodward, J. P. L. C. Salazar, L. R. Collins, and H. Meng, "Dissipation rate estimation from PIV in zero-mean isotropic turbulence," Exp. Fluids **46**(3), 499–515 (2009).
[39]W. Hwang and J. K. Eaton, "Creating homogeneous and isotropic turbulence without a mean flow," Exp. Fluids **36**(3), 444–454 (2004).
[40]Z. Dou, *Experimental Study of Inertial Particle-Pair Relative Velocity in Isotropic Turbulence* (State University of New York at Buffalo, Ann Arbor, 2017), p. 175.
[41]Y. Sun, H. Qi, G. Zhang, and Y. Wu, "Development and validation of a turbulence model based on drift velocity," Phys. Fluids **36**(12), 125166 (2024).
[42]Y. Sun, H. Qi, G. Zhang, and Y. Wu, "A novel dynamic subgrid-scale model based on partial-averaged velocity for large eddy simulation," Phys. Fluids **36**(2), 025114 (2024).
[43]Y. Wu, J. Zhang, P. J. Smith, H. Zhang, C. Reid, J. Lv, and G. Yue, "Three-dimensional simulation for an entrained flow coal slurry gasifier," Energy Fuels **24**(2), 1156–1163 (2010).
[44]C. D. Argyropoulos and N. C. Markatos, "Recent advances on the numerical modelling of turbulent flows," Appl. Math. Modell. **39**(2), 693–732 (2015).
[45]T. de Karman and L. Howarth, "On the statistical theory of isotropic turbulence," Proc. R. Soc. London, Ser. A **164**(917), 192–215 (1938).
[46]H. Shen, *Development and Application of Large Eddy Simulation for Coal Combustion* (Tsinghua University, 2020).